

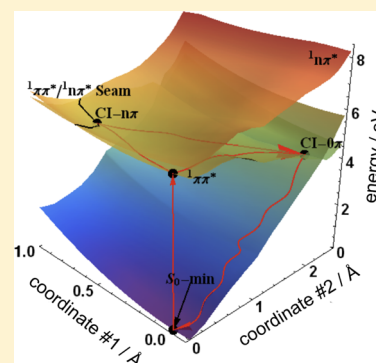
Excited-State Deactivation Pathways in Uracil versus Hydrated Uracil: Solvatochromatic Shift in the  $^1n\pi^*$  State is the Key

Xing Zhang and John M. Herbert\*

Department of Chemistry and Biochemistry, The Ohio State University, Columbus, Ohio 43210, United States

## S Supporting Information

**ABSTRACT:** Excited-state deactivation mechanisms of uracil are investigated using spin-flip time-dependent density functional theory. Two important minimum-energy crossing points are located, for both gas-phase and hydrated uracil, and optimized relaxation pathways connecting the most important critical points on the  $^1n\pi^*$  and  $^1\pi\pi^*$  potential energy surfaces are determined. An ultrafast decay time constant, measured via femtosecond spectroscopy, is assigned to direct  $^1\pi\pi^* \rightarrow S_0$  deactivation, while a slower decay component is assigned to indirect  $^1\pi\pi^* \rightarrow ^1n\pi^* \rightarrow S_0$  deactivation. The shorter lifetime of the dark  $^1n\pi^*$  state in aqueous solution is attributed to a decrease in the energy barrier along the pathway connecting the  $^1n\pi^*$  minimum to a  $^1\pi\pi^*/S_0$  conical intersection. This barrier arises due to hydrogen bonding between uracil and water, leading to a blue-shift in the  $S_0 \rightarrow ^1n\pi^*$  excitation energy and considerable modification of energy barriers on the  $^1n\pi^*$  potential surface. These results illustrate how hydrogen bonding to the chromophore can significantly impact excited-state dynamics and also highlight that relaxation pathways can be elucidated using low-cost methods based on density functional theory.



## I. INTRODUCTION

Upon excitation by UV light, DNA may form harmful photoproducts than can cause lethal carcinogenesis, though the probability of photodamage is significantly reduced due to the self-repairing system in living organisms. All five nucleobases, which are fundamental functioning parts of DNA and RNA, can relax back to their respective ground states within a few picoseconds following photoexcitation,<sup>1,2</sup> which may be an important photoprotection mechanism.

There has been significant effort in the past decade to study the excited-state deactivation mechanisms of the nucleobases, both experimentally and computationally. In particular, excited-state lifetimes of the nucleobases in both the gas phase<sup>3</sup> and in aqueous solution<sup>4</sup> are available from time-resolved spectroscopy. Although there is some disagreement regarding the precise time constants,<sup>5,6</sup> the existence of fast and slow decay components in nucleobases is now widely accepted.

Despite the availability of such data, however, the details of the excited-state dynamics in assemblies of nucleobases remain to be revealed by theoretical studies. For the individual nucleobases, vertical and/or adiabatic excitation energies, conical intersection structures, and relaxation pathways have been calculated at various levels of theory,<sup>7–10</sup> and some excited-state dynamics simulations have been performed as well.<sup>11–14</sup> Where multireference methods have been employed, computational constraints limit the system size to not much more than 15 atoms. Moreover, the use of small basis sets and insufficiently large active spaces makes the reliability (for qualitatively different excited states) and accuracy (due to the limited treatment of dynamical correlation) questionable in some cases. While the importance of dynamical correlation

beyond the complete active space, self-consistent field (CASSCF) model was pointed out long ago<sup>15</sup> and has been investigated in detail for uracil,<sup>8</sup> it is difficult to extend such high-level treatments to much larger systems.

Time-dependent density functional theory (TDDFT) is an attractive alternative due to its low computational cost. However, this method cannot correctly describe the topology of conical intersections involving the reference state,<sup>16</sup> at least not within the ubiquitous adiabatic approximation for the exchange-correlation kernel. Thus, the description of the potential surface in the important “funnel” region of near-degeneracy is highly suspicious in conventional TDDFT. A potential remedy, which is exploited in the present work, is to use the “spin-flip” (SF) generalization of TDDFT,<sup>17–19</sup> which was originally developed to investigate diradicals with strong static correlation in their ground states, which therefore makes the ground state a poor reference state. In the present context, SF-TDDFT based upon a high-spin triplet reference state affords a route to the singlet manifold, in which  $S_0$  is treated on an equal footing with the singlet excited states. As such, the description of conical intersections among singlet states poses no fundamental problem.<sup>16</sup> Good performance of SF-TDDFT for conical intersections in ethylene-like molecules has recently been reported,<sup>20–23</sup> although concerns about the suitability of choosing the lowest triplet state as the reference have also been raised.<sup>24</sup>

**Special Issue:** James L. Skinner Festschrift

**Received:** December 10, 2013

**Revised:** January 13, 2014

**Published:** January 15, 2014

Here, we apply SF-TDDFT to study the excited-state deactivation of uracil in both the gas phase and in aqueous solution. This is a system that has been studied previously, by both theory and experiment, which makes it a useful test case for evaluating the efficacy of SF-TDDFT for studies of excited-state dynamics in larger nucleic acid systems. Several decay pathways have been suggested for photoexcited uracil, namely, (1) early trapping in a shallow local minimum on the lowest  $^1\pi\pi^*$  state;<sup>11,12</sup> (2) direct internal conversion from the lowest  $^1\pi\pi^*$  state to  $S_0$ ;<sup>4</sup> (3) intersystem crossing from the lowest  $^1n\pi^*$  state to the lowest  $^3\pi\pi^*$  state;<sup>4</sup> and finally, (4) trapping on the lowest  $^1n\pi^*$  state followed by internal conversion to  $S_0$ .<sup>4</sup>

In particular, mechanisms 2–4 were proposed in an ultrafast spectroscopic study of aqueous 1-cyclohexyluracil;<sup>4</sup> the diagram in Figure 1 illustrates the bifurcated decay mechanism put forth in that study.

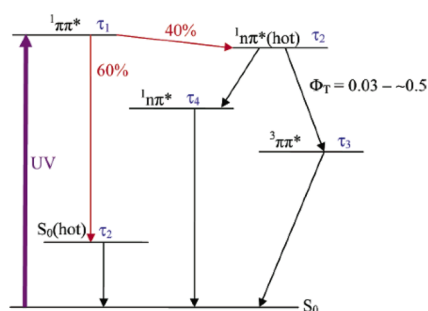


**Figure 1.** Proposed mechanism for excited-state deactivation of photoexcited 1-cyclohexyluracil, from the experimental study in ref 4. Reprinted with permission from ref 4. Copyright 2006 American Chemical Society.

In a previous computational study of uracil itself,<sup>9</sup> a conical intersection between  $S_0$  and the  $^1n\pi^*$  state was located but found to be separated by a barrier of  $\approx 1.6$  eV from the  $^1n\pi^*$  minimum. Meanwhile, a significant discrepancy exists in the experimentally reported lifetime for the spectroscopically dark  $^1n\pi^*$  state in the gas phase: several nanoseconds, according to UV spectroscopy,<sup>3,25</sup> but only 2.4 ps according to time-resolved photoelectron spectroscopy.<sup>6</sup> However, nonadiabatic *ab initio* molecular dynamics simulations of gas-phase uracil<sup>11,12</sup> suggest a different origin for a 2.4 ps time constant, namely, a combination of trapping in a shallow minimum on the  $^1\pi\pi^*$  state (1.5 ps) followed by trapping on the  $^1n\pi^*$  state ( $>1.0$  ps).<sup>12</sup> It has also been suggested that the 2.4 ps time component could result from vibrational cooling of a hot  $S_0$  state that is populated on an ultrafast time scale, whereas the lifetime of the  $^1n\pi^*$  state might be longer still.<sup>4,9</sup> For uracil in aqueous solution, the same lifetime is reported to be  $\approx 24$  ps (or 26 ps for 1-cyclohexyluracil).<sup>26</sup>

Various electronic structure methods have been deployed to study the excited-state deactivation of gas-phase uracil,<sup>7,11,12,27</sup> but only a few TDDFT calculations are available for solvated uracil.<sup>9,14,28–30</sup> Multireference wave function calculations of a binary uracil–water complex,<sup>27</sup> as well as TDDFT calculations of larger uracil–water clusters,<sup>9</sup> support the role of the  $^1n\pi^*$  as a “trap” along the  $^1\pi\pi^* \rightarrow S_0$  relaxation pathway (see Figure 1). However, conical intersections have yet to be located at the TDDFT level, owing to the fundamental limitations of traditional, spin-conserving TDDFT, and minimum-energy pathways have not been reported with either TDDFT or wave function methods.

The present work aims for a detailed comparison between decay mechanisms for uracil in the gas phase and in aqueous solution. Due to theoretical limitations, we only consider singlet states of uracil, but note that intersystem crossing has been shown to play a minor role in the decay process, as supported by the relatively low quantum yield of the  $^3\pi\pi^*$  state in solution-phase uracil ( $<10\%$  in protic solvents).<sup>4,31</sup> The crossing region between the  $^1n\pi^*$  and  $S_0$  states is also excluded from the current study, due to the large barrier along the reaction path that was determined previously.<sup>9</sup> Recently, a ring-opening conical intersection between  $S_0$  and a  $\sigma_{n\pi}\pi^*$  state, which may contribute to a new decay channel, was located computationally.<sup>12</sup> However, the overestimated stability of the ring-opening conformation in the CASSCF calculations of ref 12, along with the low fraction of the trajectories that proceed via this pathway, make it questionable whether this is really important. This pathway is not considered in the present work.

## II. METHODS

**1. Spin-Flip TDDFT.** In the present work, we use the “collinear” form of spin-flip TDDFT, first introduced by Shao et al.,<sup>17</sup> to determine excited-state relaxation pathways for uracil. (A “non-collinear” formulation of SF-TDDFT, introduced by Wang and Ziegler,<sup>18</sup> will be tested for some single-point calculations.) In the linear-response (LR) TDDFT approach, the non-Hermitian eigenvalue equation

$$\begin{pmatrix} \mathbf{A} & \mathbf{B} \\ \mathbf{B}^* & \mathbf{A}^* \end{pmatrix} \begin{pmatrix} \mathbf{X} \\ \mathbf{Y} \end{pmatrix} = \omega \begin{pmatrix} \mathbf{1} & \mathbf{0} \\ \mathbf{0} & -\mathbf{1} \end{pmatrix} \begin{pmatrix} \mathbf{X} \\ \mathbf{Y} \end{pmatrix} \quad (1)$$

is solved for the excitation energies,  $\omega$ . Here,

$$A_{ia,jb} = (\epsilon_a - \epsilon_i)\delta_{ij}\delta_{ab} + \langle ib|a|j \rangle - C_{\text{HF}}\langle ib|j|a \rangle + \langle ib|f^{\text{xc}}|aj \rangle \quad (2)$$

and

$$B_{ia,jb} = \langle ij|lab \rangle - C_{\text{HF}}\langle ij|b|a \rangle + \langle ij|f^{\text{xc}}|lab \rangle \quad (3)$$

The labels  $i, j, \dots$  and  $a, b, \dots$  represent occupied and virtual spin orbitals, respectively, and  $C_{\text{HF}}$  is the fraction of Hartree–Fock exchange included in the exchange–correlation functional. Within the SF-TDDFT method, a high-spin ( $M_S = 1$ ) triplet state is chosen as the reference state, and only the  $\alpha \rightarrow \beta$  spin excitation blocks in LR-TDDFT are used to obtain  $M_S = 0$  for the target state. As a consequence, eqs 2 and 3 reduce to the following form when using a collinear exchange–correlation functional kernel:

$$A_{ia,jb} = (\epsilon_a - \epsilon_i)\delta_{ij}\delta_{ab} - C_{\text{HF}}\langle ib|j|a \rangle \quad (4)$$

$$B_{ia,jb} = 0 \quad (5)$$

Thus, the collinear SF-TDDFT just looks like LR-TDDFT within the Tamm–Dancoff approximation, and only the Hermitian eigenvalue equation  $\mathbf{A}\mathbf{X} = \omega\mathbf{X}$  needs to be solved.

**2. Minimum-Energy Crossing Point Optimization.** To minimize the energy along a conical seam between electronic states  $I$  and  $J$ , we need the difference gradient vector

$$\mathbf{g}^{IJ} = \hat{\nabla}_R(E_I - E_J) \quad (6)$$

along with the nonadiabatic coupling vector

$$\mathbf{h}^{IJ} = \langle \Psi_I | \hat{\nabla}_R | \Psi_J \rangle \quad (7)$$

Together, these vectors define the two-dimensional branching space for the conical intersection between states  $I$  and  $J$ . Since the nonadiabatic coupling vector is not available at present for the SF-TDDFT method, we adopt the branching-plane updating approach to numerically approximate the exact branching space.<sup>32</sup> In this method, the branching plane is updated iteratively; the (approximate) branching space at step  $k$  is spanned by the normalized difference gradient vector, which we denote as  $\mathbf{x}_k$ , and another unit vector  $\mathbf{y}_k$  that is orthogonal to  $\mathbf{x}_k$ . The vector  $\mathbf{y}_k$  is defined as a linear combination of  $\mathbf{x}_{k-1}$  and  $\mathbf{y}_{k-1}$ ,

$$\mathbf{y}_k = a\mathbf{x}_{k-1} + b\mathbf{y}_{k-1} \quad (8)$$

such that  $a^2 + b^2 = 1$ . Since we require that  $\mathbf{x}_k \cdot \mathbf{y}_k = 0$ , one may solve for  $\mathbf{y}_k$ :

$$\mathbf{y}_k = \frac{(\mathbf{y}_{k-1} \cdot \mathbf{x}_k)\mathbf{x}_{k-1} - (\mathbf{x}_{k-1} \cdot \mathbf{x}_k)\mathbf{y}_{k-1}}{[(\mathbf{y}_{k-1} \cdot \mathbf{x}_k)^2 + (\mathbf{x}_{k-1} \cdot \mathbf{x}_k)^2]^{1/2}} \quad (9)$$

The gradient projection method<sup>33,34</sup> is used to optimize the structures of conical intersections. Optimization proceeds along the gradient vector

$$\mathbf{g} = 2(E_I - E_J)\mathbf{x} + \mathbf{P}\mathbf{g}_{\text{mean}} \quad (10)$$

where

$$\mathbf{P} = \mathbf{1} - \mathbf{x}\mathbf{x}^T - \mathbf{y}\mathbf{y}^T \quad (11)$$

is a projection operator onto the (approximate) seam space and

$$\mathbf{g}_{\text{mean}} = \frac{1}{2}\hat{\nabla}_R(E_I + E_J) \quad (12)$$

We find this method to be much more effective than the penalty-constrained minimization of  $\mathbf{g}_{\text{mean}}$  that has been used in some previous studies,<sup>16,20,21,35</sup> and which we had originally implemented. In addition, the plane defined by the vectors  $\mathbf{x}_k$  and  $\mathbf{y}_k$  approaches the exact branching plane very quickly after several iterations when the optimization reaches the crossing seam between states  $I$  and  $J$ .

**3. Computational Details.** In the present study, minimum-energy conical intersections and excited state relaxation pathways of uracil are calculated using SF-TDDFT in conjunction with the BH&HLYP hybrid functional (50% Hartree–Fock exchange plus 50% Becke exchange<sup>36</sup> with Lee–Yang–Parr correlation<sup>37</sup>). This somewhat unusual functional has been found to afford good results in several previous SF-TDDFT studies,<sup>17,20</sup> although it has been suggested that the relatively high fraction of Hartree–Fock exchange may be compensating for the absence of a noncollinear spin-flip formalism.<sup>24</sup> Therefore, as a test, we optimized six different minimum-energy crossing point (MECP) structures, for which MR-CIS structures are available in the literature.<sup>38</sup> The MR-CIS and SF-BH&HLYP geometries for these MECPs are superimposed in Figure 2 and are seen to be almost indistinguishable in most cases.

As a model of uracil in aqueous solution, we consider a (uracil)(H<sub>2</sub>O)<sub>4</sub> cluster in which H<sub>2</sub>O molecules are positioned at uracil's four hydrogen-bonding sites, as depicted in Figure 3. (Such a model has also been used in previous studies of excited states of aqueous uracil.<sup>30</sup>) In addition, a smooth version<sup>39,40</sup> of the conductor-like polarizable continuum model (C-PCM) is added in order to model bulk solvation.

Minimum-energy pathways for gas-phase uracil and hydrated uracil were optimized using the growing-string method<sup>41</sup> and

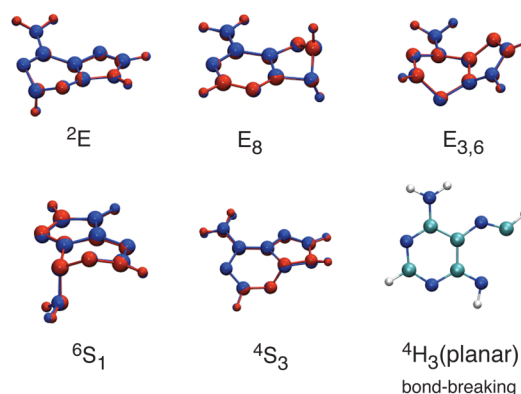


**Figure 2.** MECP structures for 9H-adenine, superimposing MR-CIS(6,5)/6-31G\* results (in red, from ref 38) with SF-BH&HLYP/6-31G\* results (in blue, this work). The nomenclature for the MECPs is taken from ref 38. The <sup>4</sup>H<sub>3</sub>(planar) MECP is not reported in ref 38 but is obtained by relaxing the (nonminimum) <sup>4</sup>H<sub>3</sub> conical intersection that is reported in that work.

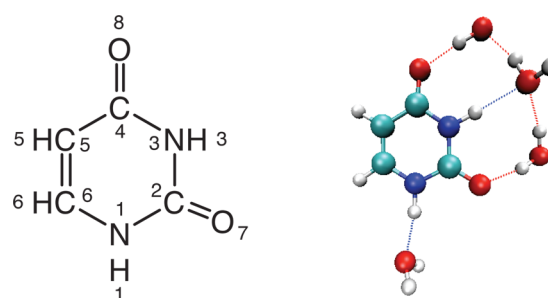


**Figure 3.** Molecular structure and numbering scheme for uracil, along with the (uracil)(H<sub>2</sub>O)<sub>4</sub> cluster that is used to model aqueous uracil.

the freezing-string method,<sup>42</sup> respectively, and coordinates for the minimum-energy critical points are available in the Supporting Information. The freezing- and growing-string methods can provide quite good approximations to exact minimum-energy pathways calculated using the intrinsic reaction coordinate method, but at lower computational cost in terms of the number of energy and gradient evaluations that are required to determine the path.<sup>42</sup> Mass-weighted coordinates were computed by setting the starting-point structure of each string as the origin.

SF-BH&HLYP/6-31+G(d,p) was used for all gradient calculations, and energetics along the relaxation pathways were then recalculated using the aug-cc-pVTZ basis set to confirm the reliability of the small basis set that is used for optimizations. The difference in energetics between the two basis sets is found to be less than 0.1 eV along the whole of each pathway, so the aug-cc-pVTZ results are omitted here. In addition, noncollinear (NC) SF- $\omega$ PBEh/6-31+G(d,p) calculations were performed along pathways optimized as indicated above, using the NC formalism of Wang and Ziegler<sup>18,19</sup> in conjunction with the long-range corrected hybrid PBE functional, LRC- $\omega$ PBEh.<sup>43</sup> (The parameters  $C_{\text{HF}} = 0.2$  and  $\omega = 0.2 \text{ bohr}^{-1}$  are used in LRC- $\omega$ PBEh, as suggested in ref 43.) Finally, RI-CC2/aug-cc-pVTZ calculations (approximate coupled-cluster theory in a resolution-of-identity implementation) were performed along the relaxation pathways obtained using SF-BH&HLYP. In general, good agreement is found among the energetics predicted by all of these methods, as demonstrated below.

Table 1. Stationary Point Geometries of Gas-Phase Uracil

parameter	$S_0$ -min		$S_{n\pi^*}$ -min		$ci-n\pi$		$ci-n\pi$ -p		$ci-0\pi$	
	DFT <sup>a</sup>	expt <sup>b</sup>	DFT <sup>a</sup>	CASSCF <sup>c</sup>	DFT <sup>a</sup>	CASSCF <sup>c</sup>	DFT <sup>a</sup>	MRCI <sup>d</sup>	DFT <sup>a</sup>	CASSCF <sup>c</sup>
C <sub>2</sub> –N <sub>3</sub>	1.372	1.373	1.388	1.378	1.369	1.371	1.421	1.335	1.372	1.358
C <sub>2</sub> –N <sub>1</sub>	1.377	1.379	1.356	1.369	1.399	1.415	1.419	1.410	1.417	1.421
C <sub>6</sub> –N <sub>1</sub>	1.367	1.380	1.409	1.405	1.350	1.337	1.313	1.330	1.346	1.325
C <sub>5</sub> –C <sub>6</sub>	1.341	1.338	1.365	1.408	1.479	1.500	1.517	1.511	1.432	1.447
C <sub>4</sub> –N <sub>3</sub>	1.395	1.383	1.385	1.393	1.420	1.432	1.469	1.462	1.421	1.433
C <sub>4</sub> –C <sub>5</sub>	1.456	1.440	1.364	1.364	1.372	1.382	1.390	1.415	1.468	1.487
C <sub>4</sub> –O <sub>8</sub>	1.205	1.227	1.385	1.361	1.255	1.252	1.195	1.205	1.199	1.194
C <sub>2</sub> –O <sub>7</sub>	1.206	1.218	1.209	1.200	1.205	1.197	1.216	1.216	1.200	1.199
∠N <sub>1</sub> C <sub>2</sub> O <sub>7</sub>	122.6	123.2	124.6	123.3	121.1	120.2	115.4	116	120.3	119.2
∠N <sub>3</sub> C <sub>4</sub> O <sub>8</sub>	120.4	119.9	111.3	113.2	115.9	115.3	116.4	116	119.2	117.7
∠N <sub>1</sub> C <sub>6</sub> C <sub>5</sub>	121.9	122.8	119.2	118.1	113.5	113.4	113.8	114	115.0	118.1
∠C <sub>4</sub> C <sub>5</sub> C <sub>6</sub>	119.6	119.2	117.7	117.8	116.6	114.4	119.5	122	114.3	110.4
∠N <sub>1</sub> C <sub>2</sub> N <sub>3</sub>	113.7	114.8	114.3	114.8	113.6	113.2	114.6		115.0	114.7
∠C <sub>2</sub> N <sub>3</sub> C <sub>4</sub>	127.8	127.0	122.3	122.7	121.2	119.2	119.3		126.1	126.4
∠N <sub>3</sub> C <sub>4</sub> C <sub>5</sub>	113.7	114.7	121.8	121.7	116.1	115.2	121.2		110.4	111.3
∠C <sub>4</sub> C <sub>5</sub> C <sub>6</sub> H <sub>5</sub>	180.0	180.0	180.0	180.0	−161.1	−139.8	180.0	180	120.8	111.7
∠C <sub>6</sub> C <sub>5</sub> C <sub>4</sub> H <sub>6</sub>	0.0	0.0	0.0	0.0	−12.3	−12.3	0.0	0	23.4	20.9
∠C <sub>4</sub> C <sub>5</sub> C <sub>6</sub> N <sub>1</sub>	0.0	0.0	0.0	0.0	−35.2	−41.2	0.0	0	53.3	51.5
∠N <sub>1</sub> C <sub>2</sub> N <sub>3</sub> C <sub>4</sub>	0.0	0.0	0.0	0.0	−28.6	−36.7	0.0	0	22.3	15.4

<sup>a</sup>SF-BH&HLYP/6-31+G(d,p) results (this work). <sup>b</sup>Experimental values are obtained by averaging over dimensions found in crystal structures.<sup>47</sup>  
<sup>c</sup>SA-3-CASSCF(10,8)/6-31G\* results, from ref 12. <sup>d</sup>MRCI1/cc-pVDZ results, from ref 7.

RI-CC2 results were obtained using the TURBOMOLE package<sup>44</sup> and all other calculations were carried out using a locally modified version of Q-Chem.<sup>45,46</sup>

### III. RESULTS AND DISCUSSION

In this section, the results of SF-BH&HLYP calculations for photophysics of uracil are presented. Stationary-point structures and their energetics are discussed first; the corresponding Cartesian coordinates can be found in the Supporting Information. Next, relaxation pathways optimized by string methods are reported. Finally, deactivation mechanisms for photoexcited uracil are proposed based on the relaxation pathways. Throughout this work, the equilibrium structures of  $S_0$  and the lowest  $1n\pi^*$  state are denoted as  $S_0$ -min and  $S_{n\pi^*}$ -min, respectively.

**A. Vertical Excitation Energies. 1. Gas Phase Uracil.** The  $S_0$ -min geometry of gas phase uracil is planar, and the geometric parameters are presented in Table 1 (The labeling of atoms is shown in Figure 3.) The  $S_0$ -min optimized by SF-BH&HLYP agrees well with the crystallographic structure,<sup>47</sup> with differences within 0.03 Å for bond lengths and 1.5° for bond angles.

Vertical excitation energies for the lowest two singlet states are presented in Table 2. The  $S_1$  state with  $A''$  symmetry has  $n\pi^*$  character (excitation from the  $n_{O8}$  lone pair into a  $\pi^*$  orbital), and the  $S_2$  state with  $A'$  symmetry is a bright  $\pi\pi^*$  state. An exhaustive theoretical study of these vertical excitation energies was reported in ref 8, and the best theoretical estimate from that study is probably the CR-EOM-CCSD(T)/aug-cc-pVTZ result, at 5.00 eV for the  $S_1$  state and 5.25 eV for the  $S_2$  state. Our SF-BH&HLYP excitation energies are  $\approx 0.6$  eV higher, although the energy gap between  $S_1$  and  $S_2$  ( $\approx 0.3$  eV) is in good agreement with the CR-EOM-CCSD(T) result. This lends some credence to the excited-state relaxation pathways described in the next section. We also note that the noncollinear formalism<sup>18,19</sup> for SF-TDDFT improves the vertical excitation energies by about 0.4 eV, relative to the CR-EOM-CCSD(T) benchmark. It may be interesting to

Table 2. Vertical Excitation Energies (in eV) for the First Two Singlet Excited States of Gas-Phase Uracil

method	$1^1A''$ ( $n\pi^*$ )	$1^1A'$ ( $\pi\pi^*$ )
SF-BH&HLYP/6-31+G(d,p)	5.60	5.93
SF-BH&HLYP/aug-cc-pVTZ	5.54	5.84
NC-SF- $\omega$ PBEh/aug-cc-pVTZ	5.15	5.55
EOM-CCSD/6-311++G(d,p)	5.26	5.75
CR-EOM-CCSD(T) <sup>a</sup>	5.00	5.25
MS-CASPT2 <sup>b</sup>	5.05	5.78
TD-PBE0 <sup>c</sup>	4.80	5.26
RI-CC2 <sup>d</sup>	4.80	5.35
MRCI $\sigma\pi$ <sup>e</sup>	4.80	5.79

<sup>a</sup>CR-EOM-CCSD(T)/aug-cc-pVTZ, from ref 8. <sup>b</sup>MS-3-CASPT2/SA-3-CASSCF(10,8)/6-31G\*, from ref 12. <sup>c</sup>TD-PBE0/6-311+G(2d,2p), from ref 30. <sup>d</sup>RI-CC2/aug-cc-pVQZ, from ref 48. <sup>e</sup>From ref 7.

examine the behavior of noncollinear SF-TDDFT when used to scan potential energy surfaces, but at present numerically stable analytic gradients are not available for non-LDA functionals,<sup>19</sup> so optimizing pathways is expensive and problematic.

SF-BH&HLYP optimization affords a planar minimum-energy geometry for the  $S_1$  state, which agrees with the CASSCF result<sup>12</sup> (see Table 1). A previous MRCI study, however, found a slightly puckered equilibrium geometry for  $S_1$ .<sup>7</sup> As far as we know, the potential energy surface near  $S_{n\pi^*}$ -min is quite flat, so the results may be very sensitive to small changes in the level of electronic structure theory that is used. Compared with the ground-state minimum, the C<sub>4</sub>–O<sub>8</sub> and C<sub>5</sub>–C<sub>6</sub> bonds at  $S_{n\pi^*}$ -min geometry are elongated by 0.18 and 0.03 Å, respectively, while the C<sub>4</sub>–C<sub>5</sub> bond is shortened by 0.09 Å due to excitation from the  $n_{O8}$  nonbonding orbital to an antibonding  $\pi^*$  orbital. The adiabatic excitation energy is 4.2 eV according to SF-BH&HLYP (see Table 3), in agreement with previous CASPT2 and MR-CISD results.<sup>12</sup> Unconstrained geometry optimization of the  $S_2$  state by SF-BH&HLYP leads



Table 3. Relative Energies (in eV) at Stationary Points of Gas-Phase Uracil

	$S_0$ -min		$S_{n\pi^*}$ -min		$ci$ - $n\pi$		$ci$ - $n\pi$ -p		$ci$ - $0\pi$	
	spin-flip <sup>a</sup>	RI-CC2 <sup>b</sup>	spin-flip <sup>a</sup>	RI-CC2 <sup>b</sup>	spin-flip <sup>a</sup>	RI-CC2 <sup>b</sup>	spin-flip <sup>a</sup>	RI-CC2 <sup>b</sup>	spin-flip <sup>a</sup>	RI-CC2 <sup>b</sup>
$S_0$	0.00 (0.00)	0.00	1.29 (1.03)	0.82	1.83 (1.66)	1.59	1.29 (1.15)	1.10	4.24 (4.05)	3.97
$^1n\pi^*$	5.60 (5.23)	4.96	4.16 (4.29)	3.85	5.17 (4.90)	4.73	5.84 (5.52)	5.38	7.14 (6.76)	6.48
$^1\pi\pi^*$	5.93 (5.64)	5.44	5.90 (5.42)	5.25	5.17 (4.82)	4.87	5.84 (5.48)	5.38	4.24 (4.01)	3.88

<sup>a</sup>Relative energies computed at the SF-BH&HLYP/6-31+G(d,p) level and, in parentheses, at the NC-SF- $\omega$ PBEh/6-31+G(d,p) level. Geometries are computed at the SF-BH&HLYP/6-31+G(d,p) level. <sup>b</sup>Relative energies at the RI-CC2/aug-cc-pVTZ//SF-BH&HLYP/6-31+G(d,p) level.

Table 4. Relative Energies (in eV) at Stationary Points of Hydrated Uracil

	$S_0$ -min		$S_{n\pi^*}$ -min		$ci$ - $n\pi$		$ci$ - $n\pi$ -p		$ci$ - $0\pi$	
	spin-flip <sup>a</sup>	RI-CC2 <sup>b</sup>	spin-flip <sup>a</sup>	RI-CC2 <sup>b</sup>	spin-flip <sup>a</sup>	RI-CC2 <sup>b</sup>	spin-flip <sup>a</sup>	RI-CC2 <sup>b</sup>	spin-flip <sup>a</sup>	RI-CC2 <sup>b</sup>
$S_0$	0.00 (0.00)	0.00	1.63 (1.22)	1.00	1.04 (0.92)	0.84	1.03 (0.87)	0.74	4.38 (4.18)	3.81
$^1n\pi^*$	5.80 (5.49)	5.29	6.12 (5.69)	5.37	5.38 (5.03)	4.84	5.73 (5.34)	5.06	4.38 (4.14)	4.58
$^1\pi\pi^*$	6.10 (5.68)	5.46	4.58 (4.72)	4.65	5.38 (5.07)	5.07	5.73 (5.40)	5.32	7.52 (7.16)	7.42

<sup>a</sup>Relative energies computed at the SF-BH&HLYP/6-31+G(d,p) level and, in parentheses, at the NC-SF- $\omega$ PBEh/6-31+G(d,p) level. Geometries are computed at the SF-BH&HLYP/6-31+G(d,p) level. <sup>b</sup>Relative energies at the RI-CC2/aug-cc-pVTZ//SF-BH&HLYP/6-31+G(d,p) level.

directly to the crossing region between the  $S_1$  and  $S_2$  states, a point to which we shall return later.

**2. Hydrated Uracil.** Solvatochromatic shifts in uracil have been studied previously at many different levels of theory.<sup>8,27,30,49–52</sup> Most studies show that the order of the lowest  $^1\pi\pi^*$  and  $^1n\pi^*$  states is reversed in aqueous solution, relative to that in the gas phase, with solvatochromatic shifts ranging from  $-0.1$  to  $-0.3$  eV for the  $^1\pi\pi^*$  state and from  $+0.4$  to  $+0.5$  eV for the  $^1n\pi^*$  state, depending on the level of theory. Our SF-BH&HLYP/C-PCM results for the microhydrated (uracil)(H<sub>2</sub>O)<sub>4</sub> system agree well with the previous studies: the energy shifts are  $-0.13$  eV for the  $^1\pi\pi^*$  state and  $0.50$  eV for the  $^1n\pi^*$  state (see Table 4).

The equilibrium geometry of the ground state is planar and similar to the gas-phase geometry. The major difference is that the two C–O bonds are  $\approx 0.02$  Å longer for hydrated uracil, which is caused by the hydrogen bonding interaction with the nearby water molecules, and this phenomenon manifests in the other stationary-point structures as well. We also optimized the equilibrium structure of the  $^1n\pi^*$  state and found that it deviates slightly from the planar geometry via ring puckering. The adiabatic excitation energy is reported in Table 4 as  $4.6$  eV, which represents a solvatochromatic blue-shift of  $0.4$  eV relative to gas-phase uracil, but we will see below that the energy barriers on the  $^1n\pi^*$  state are smaller in the hydrated system, despite its larger vertical excitation energy. Unconstrained geometry optimization of the  $^1\pi\pi^*$  state directly leads to the crossing region between the  $^1\pi\pi^*$  and the  $S_0$  states, indicating little if any barrier between the  $S_1$  minimum and the  $S_1/S_0$  conical intersection of hydrated uracil, at the SF-BH&HLYP level of theory.

Regarding the solvation structure upon electronic excitation: upon  $S_0 \rightarrow ^1n\pi^*$  excitation and subsequent relaxation to the  $S_{n\pi^*}$ -min geometry, we find that the water molecule hydrogen-bonded to O<sub>8</sub> moves out of the uracil plane, and the hydrogen bond lengthens by  $0.2$  Å. This is mainly caused by the  $n_{O_8} \rightarrow \pi^*$  character of the excitation.

**B. Conical Intersections.** In the present study, we consider only the two most important MECPs that determine the main deactivation channels of uracil. The conical intersection between the  $^1\pi\pi^*$  and  $^1n\pi^*$  states is denoted  $ci$ - $n\pi$ , and the one between the  $^1\pi\pi^*$  and  $S_0$  states is denoted  $ci$ - $0\pi$ . Relative

energies at these geometries are listed in Tables 3 and 4. Optimized structures in the gas phase are depicted in Figure 4, and the ones for hydrated uracil are quite similar.

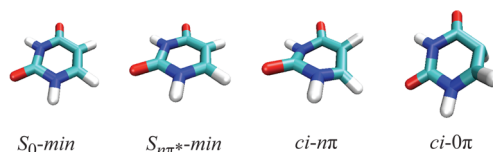


Figure 4. Structures optimized at the SF-BH&HLYP/6-31+G(d,p) level for gas-phase uracil. Similar critical points are obtained for hydrated uracil.

**1.  $ci$ - $n\pi$ .** The  $ci$ - $n\pi$  intersection has a boat conformation with the two oxygen atoms pointing away from the ring in the same direction. For gas-phase uracil, the energy of the  $^1\pi\pi^*$  state is  $0.76$  eV lower at  $ci$ - $n\pi$  than the energy at the  $S_0$  geometry, according to the SF-BH&HLYP/6-31+G(d,p) method; this energy difference is  $0.78$  eV for NC-SF- $\omega$ PBEh/6-31+G(d,p) and  $0.64$  for RI-CC2/aug-cc-pVTZ calculations. For the hydrated uracil case, the energy lowering is  $0.42$  eV,  $0.44$  eV, and  $0.34$  eV, respectively, for these three methods (see Tables 3 and 4). Thus, the system always goes downhill to reach  $ci$ - $n\pi$  from the Franck–Condon (FC) region, for both gas-phase and hydrated uracil. Although the NC version of SF-TDDFT systematically moves the excitation energies closer to RI-CC2 results (see Tables 3 and 4), most of the discrepancy between excitation energies computed with all three methods reflects the energy difference relative to the ground state. Later, when we discuss the details of the relaxation process, we will see that all three methods afford similar energetics across the relaxation pathway.

Finally, we also optimized the structure of the planar conical intersections (labeled as  $ci$ - $n\pi$ -p) between the  $^1\pi\pi^*$  and the  $^1n\pi^*$  states for both gas-phase and hydrated uracil. The geometry of this symmetry-constrained MECP in the gas phase agrees with the one obtained at the MRCI level in ref 7; see Table 1. The change in energy in moving from the FC region of the  $^1\pi\pi^*$  state to  $ci$ - $n\pi$ -p is  $-0.09$  eV in the gas phase [SF-BH&HLYP/6-31+G(d,p) level], as compared to  $-0.14$  eV [NC-SF- $\omega$ PBEh/6-31+G(d,p)] and  $-0.06$  eV (RI-CC2/aug-

cc-pVTZ). For hydrated uracil, the same energy changes are  $-0.07$ ,  $-0.12$ , and  $-0.10$  eV, respectively. Thus, the  $^1\pi\pi^*$  state energy at the *ci-n $\pi$ -p* geometry is slightly lower in energy ( $\approx 0.1$  eV), or perhaps comparable to, the energy of the  $^1\pi\pi^*$  state in the FC region. The potential importance of this conical intersection is discussed in the next section.

**2. *ci-0 $\pi$* .** The *ci-0 $\pi$*  intersection has an ethylenic structure with pyramidalization at the C<sub>5</sub> atom and out-of-plane distortion at H<sub>5</sub> (see Figure 4). The energies of *ci-0 $\pi$*  are 4.24 and 4.38 eV higher than the  $S_0$ -min energies for gas-phase uracil and hydrated uracil, respectively [SF-BH&HLYP/6-31+G(d,p) level], due to significant distortion away from a planar geometry. In the NC-SF- $\omega$ PBEh calculations, these energy differences are reduced to 4.03 eV (gas phase) and 4.16 eV (hydrated), and the RI-CC2 results are 3.92 eV (gas phase) and 4.20 eV (hydrated). We note that the energy gap between the  $S_0$  state and the  $^1\pi\pi^*$  state at *ci-0 $\pi$*  geometry for hydrated uracil is quite large in the RI-CC2 calculation (0.77 eV). This means that the crossing point between these two states in the RI-CC2 calculation is a little different from *ci-0 $\pi$*  optimized by SF-BH&HLYP. However, the relaxation pathways calculated by the two methods agree well with each other, as demonstrated in the next section.

**C. Relaxation Pathways.** In this section, we present optimized minimum-energy relaxation pathways connecting the critical points reported in the last section, with the aim of unraveling the excited-state deactivation mechanism(s).

**1. Ultrafast Internal Conversion between the  $^1\pi\pi^*$  and  $S_0$  States.** Immediately after photoexcitation to the first  $^1\pi\pi^*$  state at the Franck–Condon geometry, the system can evolve on that excited state energy surface. Figure 5 shows the minimum-energy pathway connecting the  $S_0$ -min and *ci-0 $\pi$*  geometries for both gas-phase and hydrated uracil. No barriers on the  $^1\pi\pi^*$  state energy surfaces are found. Although we attempted to optimize the minimum-energy geometry for the  $^1\pi\pi^*$  state, this optimization led directly to the *ci-n $\pi$*  crossing region in gas phase and to the *ci-0 $\pi$*  crossing region for hydrated uracil. (Recall that the ordering of the  $^1\pi\pi^*$  and  $^1n\pi^*$  states in the FC region is different in the gas phase than in aqueous solution.) The system must encounter the *ci-n $\pi$*  funnel region in gas phase (Figure 5a), while it can bypass the *ci-n $\pi$*  funnel region when evolving on the  $^1\pi\pi^*$  state in aqueous solution (Figure 5b). This is further discussed below.

The question of whether the  $^1\pi\pi^*$  state exhibits a local minimum remains a topic of debate, and the answer changes depending on the electronic structure method that is used. A shallow minimum on the  $^1\pi\pi^*$  state, which would trap the uracil molecule on that state, is predicted in refs 11 and 12, and in those studies the slower decay component (several picoseconds) that is observed experimentally was ascribed to such trappings. The minimum-energy pathways computed here, however, along with results from attempted geometry optimizations, support the hypothesis that there does not exist any significant barrier that might trap uracil on the  $^1\pi\pi^*$  state. This conclusion is reached also in several other theoretical studies.<sup>7,9,53</sup> Moreover, fluorescence up-conversion experiments suggest a subpicosecond lifetime for the  $^1\pi\pi^*$  state,<sup>30</sup> in conflict with the suggestion that trapping occurs on that state. Thus, we assign the fastest subpicosecond decay component (called  $\tau_1$  in ref 4) of the optically populated  $^1\pi\pi^*$  state to direct internal conversion with the ground state.

**2. Role of the Long-Lived  $^1n\pi^*$  Dark State.** As discussed in the previous section, the energy of the  $^1\pi\pi^*$  state of uracil at the

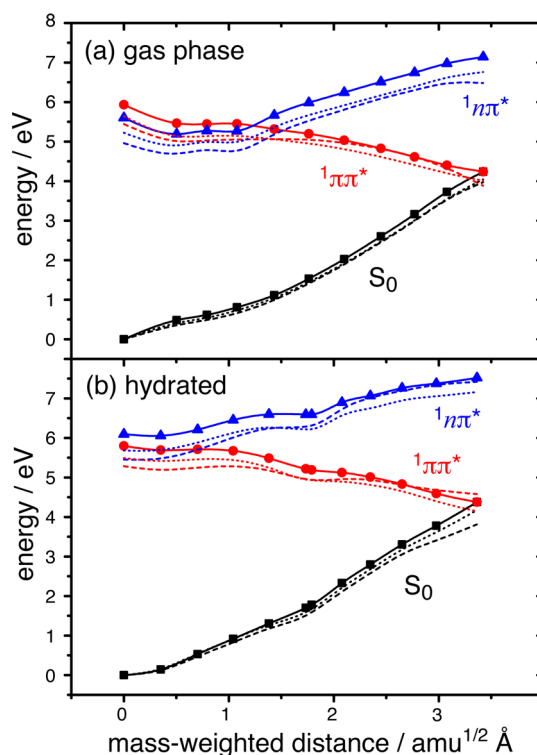


**Figure 5.** Relaxation pathways from  $S_0$ -min to *ci-0 $\pi$*  for (a) gas-phase uracil and (b) hydrated uracil, following the gradient of the  $^1\pi\pi^*$  state. Solid curves connect points along the pathway that have been optimized at the SF-BH&HLYP/6-31+G(d,p) level. Energetics along that same pathway have also been computed at the NC-SF- $\omega$ PBEh/6-31+G(d,p) level (dotted curves) and the RI-CC2/aug-cc-pVTZ level (dashed curves).

*ci-n $\pi$*  geometry is smaller than that at the Franck–Condon geometry, for both gas-phase and hydrated uracil. The crossing region near *ci-n $\pi$*  is the starting point where the  $^1n\pi^*$  state begins to contribute to the deactivation process. Figure 6 depicts minimum-energy pathways of the  $^1\pi\pi^*$  state connecting  $S_0$ -min and *ci-n $\pi$*  configurations. The reaction pathway is barrierless for gas-phase uracil (Figure 6a), while a small barrier of  $<0.1$  eV is found for hydrated uracil (Figure 6b). Although we attempted to find a local minimum on the latter pathway, geometry optimizations invariably led to the crossing region between the  $S_0$  and  $^1\pi\pi^*$  states. Meanwhile, due to the large excess energy gained by the system after photoexcitation, the small barrier predicted in the hydrated case should be easily overcome. For these reasons, we conclude that aqueous uracil excited to the  $^1\pi\pi^*$  state will evolve directly to *ci-0 $\pi$*  or to *ci-n $\pi$*  without any trapping on the  $^1\pi\pi^*$  state.

In the previous section, we mentioned the existence of a planar conical intersection (*ci-n $\pi$ -p*), for both gas-phase and hydrated uracil. The mass-weighted distances between  $S_0$ -min and *ci-n $\pi$ -p* structures are  $1.00 \text{ amu}^{1/2} \text{ Å}$  (gas phase) and  $1.07 \text{ amu}^{1/2} \text{ Å}$  (hydrated), which should be compared with the lengths of the pathways connecting  $S_0$ -min and *ci-n $\pi$*  in Figure 6, which are larger than  $2 \text{ amu}^{1/2} \text{ Å}$ . This indicates that the crossing regions between the  $^1\pi\pi^*$  state and the  $^1n\pi^*$  state are geometrically close to the FC region in both the gas phase and in solution. Keeping in mind the excess vibrational energy after photoexcitation and the fact that the  $^1\pi\pi^*$  state in both the gas-phase and hydrated case is similar between  $S_0$ -min and *ci-n $\pi$ -p*, we propose that the system can reach the crossing seam

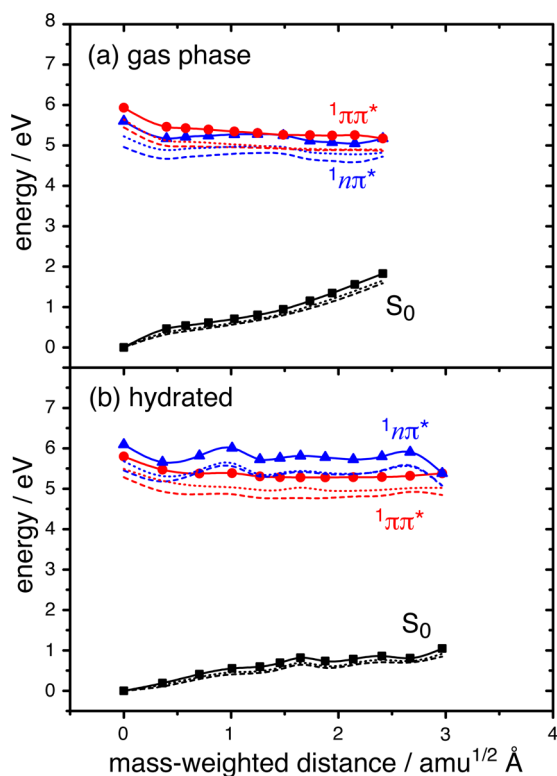


**Figure 6.** Relaxation pathways from  $S_0$ -min to  $ci-n\pi$  for (a) gas-phase uracil and (b) hydrated uracil, following the gradient of the  $1\pi\pi^*$  state. Solid curves connect points along the pathway that have been optimized at the SF-BH&HLYP/6-31+G(d,p) level. Energetics along that same pathway have also been computed at the NC-SF- $\omega$ PBEh/6-31+G(d,p) level (dotted curves) and the RI-CC2/aug-cc-pVTZ level (dashed curves).

between the  $1\pi\pi^*$  state and the  $1n\pi^*$  state very early after photoexcitation, which is associated with the subpicosecond decay component,  $\tau_1$ .

After the system encounters the intersection seam between the  $1\pi\pi^*$  and  $1n\pi^*$  states, the wave function is a mixture of  $\pi\pi^*$  and  $n\pi^*$  character. The reaction pathway may bifurcate in two directions, depending on which character the wave function takes after the system leaves the crossing region, as already shown in previous studies.<sup>7,12</sup> Examining the branching-space vectors  $\mathbf{x}$  and  $\mathbf{y}$  at the  $ci-n\pi$  geometry, which are shown in Figure 7, we see that  $\mathbf{x}$  is mainly the  $C_4-O_8$  bond stretch, which leads to  $S_{n\pi^*}$ -min, while  $\mathbf{y}$  is the  $C_4-C_5$  stretch combined with ring puckering, which leads to  $ci-0\pi$ .

If the diabatic  $\pi\pi^*$  character is maintained during the decay process, then the system will evolve directly toward  $ci-0\pi$  (see Figure 8). For the situation in the gas phase, this decay

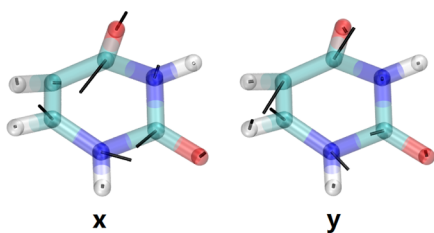


**Figure 7.** Optimized  $\mathbf{x}$  and  $\mathbf{y}$  vectors (black line segments) at the  $ci-n\pi$  conformation of gas-phase uracil.

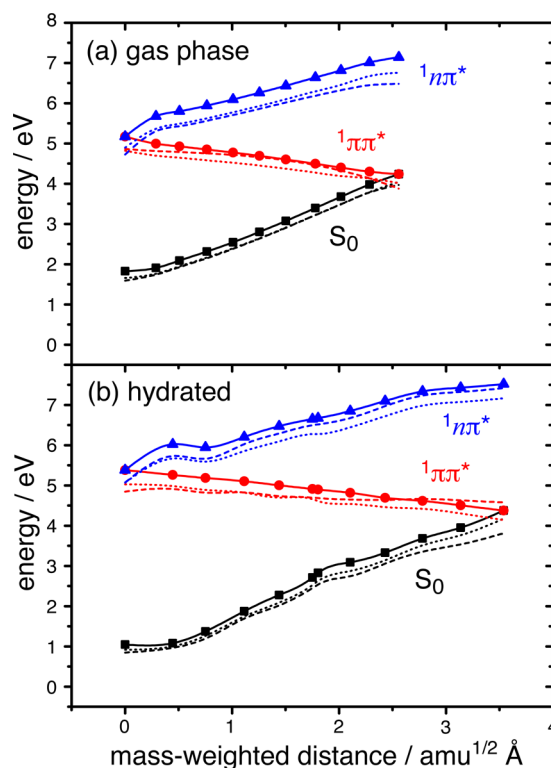


**Figure 8.** The relaxation pathways from  $ci-n\pi$  to  $ci-0\pi$  for (a) gas-phase uracil and (b) hydrated uracil, following the gradient of the  $1\pi\pi^*$  state. Solid curves connect points along the pathway that have been optimized at the SF-BH&HLYP/6-31+G(d,p) level. Energetics along that same pathway have also been computed at the NC-SF- $\omega$ PBEh/6-31+G(d,p) level (dotted curves) and the RI-CC2/aug-cc-pVTZ level (dashed curves).

component is just a part of the direct ultrafast internal conversion between the  $1\pi\pi^*$  and  $S_0$  states. Because the state ordering of  $1\pi\pi^*$  and  $1n\pi^*$  changes along the decay pathway (Figure 5a), the system has to cross the intersection seam between these two states. The situation for hydrated uracil is slightly different. In the Franck–Condon region, the  $S_1$  state has  $\pi\pi^*$  character while the  $S_2$  state has  $n\pi^*$  character. From Figure 5b, we note that the system need not encounter the crossing seam between the  $1\pi\pi^*$  and  $1n\pi^*$  states in order to decay toward  $ci-0\pi$ . Thus, the decay channel  $FC \rightarrow ci-n\pi \rightarrow ci-0\pi$  is distinct from the one in Figure 5b, namely,  $FC \rightarrow ci-0\pi$ , in the case of hydrated uracil. We next explain this conclusion.

In Figure 9, we report the minimum-energy pathways connecting  $S_0$ -min,  $ci-n\pi$  and  $ci-0\pi$ , projected onto a two-dimensional reaction coordinate plane. One direction represents the geometry change between  $S_0$ -min and  $ci-0\pi$ , defined as the direction of the vector

$$\mathbf{a} = \mathbf{R}_{ci-0\pi} - \mathbf{R}_{S_0-min} \quad (13)$$

The other direction vector represents the geometry change between  $S_0$ -min and  $ci-n\pi$ , but with the  $\mathbf{a}$  direction projected out. This corresponds to the direction of the vector

$$\mathbf{b} = (\mathbf{1} - \hat{\mathbf{a}}\hat{\mathbf{a}}^T)(\mathbf{R}_{ci-n\pi} - \mathbf{R}_{S_0-min}) \quad (14)$$

where  $\hat{\mathbf{a}} = \mathbf{a}/\|\mathbf{a}\|$ . In the gas phase, we see from Figure 9a that the paths  $FC \rightarrow ci-n\pi$  and  $ci-n\pi \rightarrow ci-0\pi$  are quite close to the path  $FC \rightarrow ci-0\pi$ , so there is essentially only one decay channel from the Franck–Condon geometry to  $ci-0\pi$ , going through the



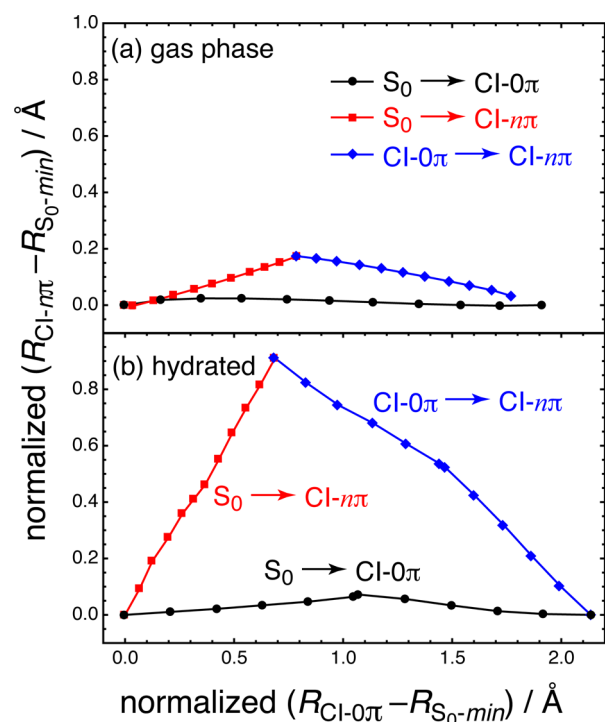


**Figure 9.** Projected relaxation pathways  $S_0$ -min  $\rightarrow$   $ci$ - $0\pi$  (black curve),  $S_0$ -min  $\rightarrow$   $ci$ - $n\pi$  (red curve), and  $ci$ - $n\pi$   $\rightarrow$   $ci$ - $0\pi$  (blue curve) for (a) gas-phase uracil and (b) hydrated uracil. The directions of the horizontal and vertical axes are defined in eqs 13 and 14, respectively.

$^1\pi\pi^*/^1n\pi^*$  intersection seam. For hydrated uracil (Figure 9b), the paths  $FC \rightarrow ci$ - $n\pi$  and  $ci$ - $n\pi \rightarrow ci$ - $0\pi$  are far away from the path  $FC \rightarrow ci$ - $0\pi$ , and combined with the pathway shown in Figure 5b, we conclude that the intersection seam between the  $^1\pi\pi^*$  and  $^1n\pi^*$  states does not lie in the same region of the potential surface as the decay channel  $FC \rightarrow ci$ - $0\pi$ .

In order to further explain the above conclusion, we did an extensive potential energy surface (PES) scan at the level of SF-BH&HLYP/6-31+G(d,p) near the three relaxation pathways shown in Figure 9. The surfaces thus obtained are shown in Figure 10. Note that the  $ci$ - $n\pi$  point shown in Figure 10b is not the real MECP on the  $^1\pi\pi^*/^1n\pi^*$  crossing seam that is depicted in Figure 4, because we did not perform geometry relaxations for the PES, but the energy increase is only 0.17 eV. Consequently, the position of the  $^1\pi\pi^*/^1n\pi^*$  crossing seam in Figure 10b represents the position of the seam through which the system can cross near the  $ci$ - $n\pi$  MECP. Comparing the PES of gas-phase uracil to that of its hydrated analogue, it is clear that the  $^1\pi\pi^*/^1n\pi^*$  crossing seam moves far away from the  $FC$  region for hydrated uracil, as a direct result of the solvatochromatic shifts for the  $^1\pi\pi^*$  and  $^1n\pi^*$  states. In Figure 10, the red curves on the  $^1\pi\pi^*$  state are the minimum relaxation pathways connecting the critical points. For gas-phase uracil, only one decay channel is found, namely,  $FC \rightarrow ^1\pi\pi^*/^1n\pi^*$  seam  $\rightarrow ci$ - $0\pi$ . For hydrated uracil, however, we observe a broad, nearly barrierless region enclosed by the three relaxation pathways on the  $^1\pi\pi^*$  state. Thus, the system is free to either evolve to the  $^1\pi\pi^*/^1n\pi^*$  crossing seam then return back to the  $^1\pi\pi^*/S_0$  seam, or directly travel toward the  $^1\pi\pi^*/S_0$  seam without reaching the  $^1\pi\pi^*/^1n\pi^*$  crossing region.

As such, there are two decay channels from the  $FC$  geometry to  $ci$ - $0\pi$  for uracil in aqueous solution, namely,  $FC \rightarrow ci$ - $0\pi$  and  $FC \rightarrow ^1\pi\pi^*/^1n\pi^*$  seam  $\rightarrow ci$ - $0\pi$ . However, since both of these

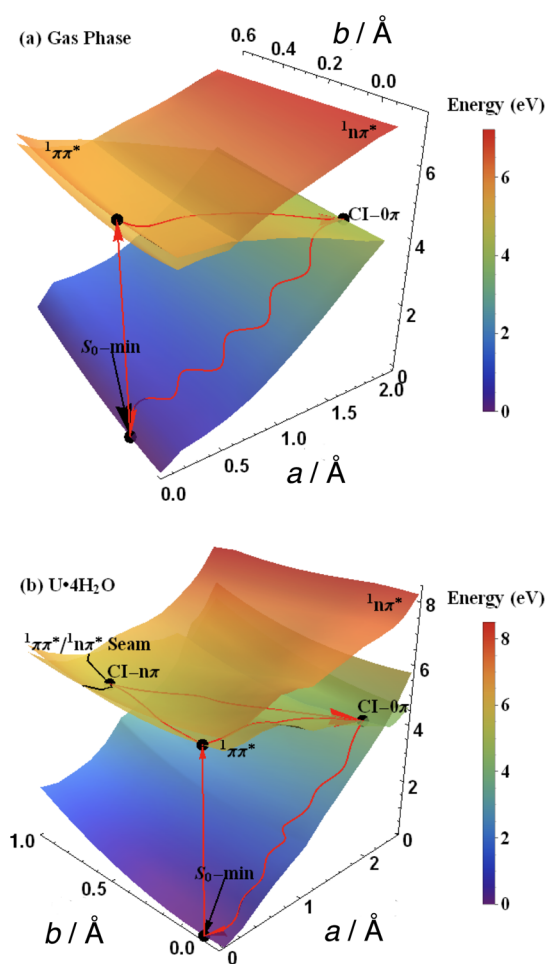


**Figure 10.** Potential energy surfaces for the lowest three singlet states for (a) gas-phase uracil and (b) hydrated uracil. The  $a$  and  $b$  axes are defined in eqs 13 and 14

two channels are downhill on the  $^1\pi\pi^*$  surface, we do not expect significantly different time constants in time-resolved experiments; both channels correspond to the fastest decay component ( $\tau_1$ ).

The wave function can also take  $n\pi^*$  character after the system encounters the  $^1\pi\pi^*/^1n\pi^*$  crossing seam. In Figure 11, we see that the system can travel on the  $^1n\pi^*$  surface in a barrierless process toward  $S_{n\pi^*}$ -min. In the solution phase, this process is associated with the vibrational cooling of the  $^1n\pi^*$  state. Because of the existence of this stable equilibrium structure ( $S_{n\pi^*}$ -min), the system can be trapped on the  $^1n\pi^*$  state for a relatively longer time ( $\tau_4$  in ref 4), from tens of picoseconds to several nanoseconds, depending on whether the solvent is protic or aprotic.

Figure 12 shows the relaxation pathways connecting  $S_{n\pi^*}$ -min and  $ci$ - $0\pi$ . In order to go back to the crossing region between the  $^1\pi\pi^*$  and  $S_0$  states, the system has to overcome a relatively large energy barrier ( $\approx 1.0$  eV in gas phase and  $\approx 0.7$  eV for hydrated uracil at the SF-BH&HLYP level), and this is the reason for the long lifetime of the dark singlet state that is observed in time-resolved experiments. (At the NC-SF- $\omega$ PBEh level, the barrier drops from 0.61 eV for gas-phase uracil to 0.39 eV for hydrated uracil, while RI-CC2 results are 1.1 eV for gas-phase uracil and 0.4 eV for hydrated uracil.) This lowering of the barrier upon hydration may be the reason for the shorter lifetime ( $\tau_4$ ) of the singlet dark state in protic solvents as



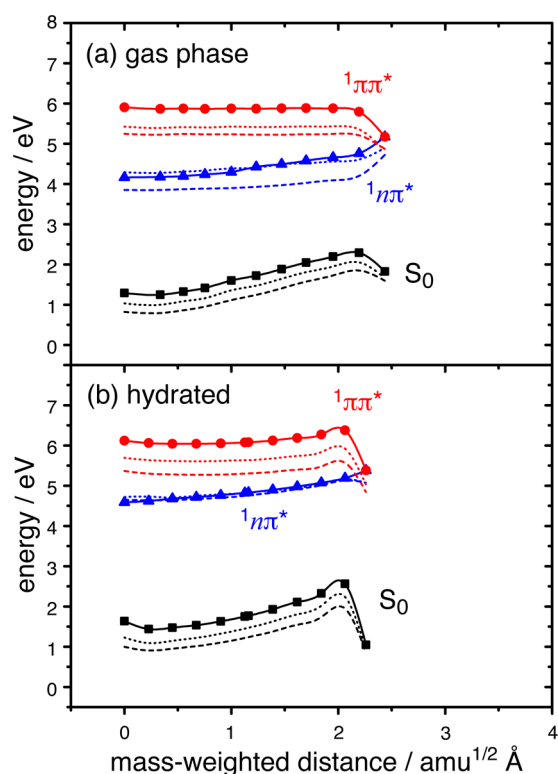


**Figure 11.** The relaxation pathways from  $S_{n\pi^*}$ -min to  $ci-n\pi$  for (a) gas-phase uracil and (b) hydrated uracil, following the gradient of the  $n\pi^*$  state. Solid curves connect points along the pathway that have been optimized at the SF-BH&HLYP/6-31+G(d,p) level. Energetics along that same pathway have also been computed at the NC-SF- $\omega$ PBEh/6-31+G(d,p) level (dotted curves) and the RI-CC2/aug-cc-pVTZ level (dashed curves).

compared to aprotic solvents.<sup>4</sup> A similar conclusion was reached in a previous TDDFT study.<sup>9</sup>

**3. Quantum Yield of the  $1n\pi^*$  State.** Transient absorption spectroscopy indicates that the quantum yield of the ultrafast internal conversion through  $ci-0\pi$  is  $\sim 60\%$  (for all solvents examined experimentally), and the remaining 40% of the quantum yield was ascribed to some combination of deactivation to the singlet  $1n\pi^*$  dark state and to the triplet  $3\pi\pi^*$  dark state.<sup>4</sup> If we assume that the  $3\pi\pi^*$  state is obtained by intersystem crossing from the  $1n\pi^*$  state, as proposed in ref 4, then the quantum yield of the  $1n\pi^*$  state can be taken as  $\sim 40\%$  after decay through the  $1\pi\pi^*/1n\pi^*$  crossing region, in all solvents.

In the present study, if we assume the deactivation mechanism of uracil in the gas phase is similar to that in aprotic solvents, where no hydrogen bonds are formed between uracil and the solvent molecules, then it is possible to study the quantum yield of the  $1n\pi^*$  state for uracil in different solvents. In the previous discussion, we saw that the major difference of the decay channels for gas-phase uracil and hydrated uracil is that the direct deactivation from the  $1\pi\pi^*$  state to the ground state through the  $ci-0\pi$  conical intersection for hydrated uracil can bypass the  $1\pi\pi^*/1n\pi^*$  crossing region. Thus, the probability for the system to reach the  $ci-n\pi$  crossing seam may be smaller for hydrated uracil. In other words, the quantum yield of the dark  $1n\pi^*$  state may be lower for uracil in protic solvents. However, this effect may be minor due to the excess energy at photoexcitation which may lead the system to the energetically

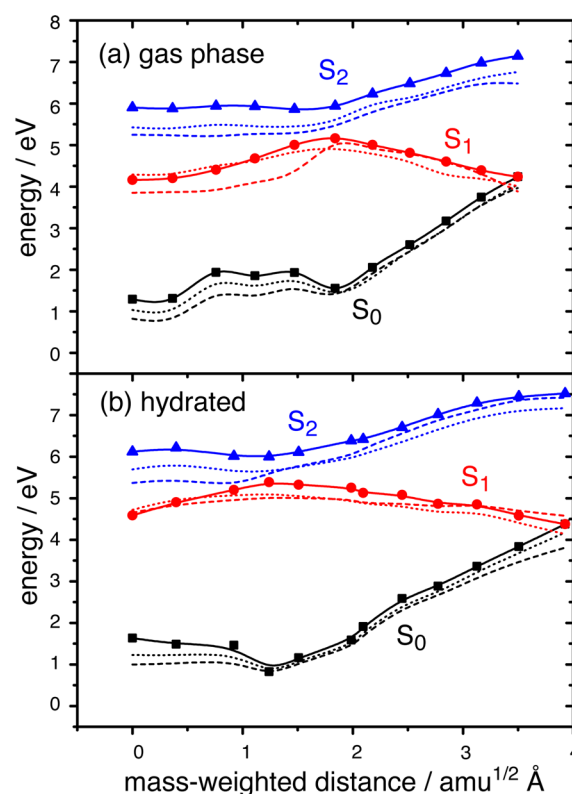


**Figure 12.** Relaxation pathways from  $S_{n\pi^*}$ -min to  $ci-0\pi$  for (a) gas-phase uracil and (b) hydrated uracil, following the gradient of the  $S_1$  state. The wave function changes character from  $n\pi^*$  to  $\pi\pi^*$  at the maximum energy point on the  $S_1$  pathway, so the reaction pathways come across the  $1\pi\pi^*/1n\pi^*$  crossing regions and lead the system back to the  $1\pi\pi^*$  surface. [Solid curves represent the pathway optimized at the SF-BH&HLYP/6-31+G(d,p) level, whereas energetics along that same pathway are also computed at the NC-SF- $\omega$ PBEh/6-31+G(d,p) level (dotted curves) and the RI-CC2/aug-cc-pVTZ level (dashed curves).]

unfavored but geometrically closer  $ci-n\pi$  crossing seam (see the discussion above regarding the  $ci-n\pi$ -p conical intersection). In any case, the quantum yield of the singlet dark state of uracil in protic solvents appears to be governed by the competition between the  $FC \rightarrow ci-0\pi$  and the  $FC \rightarrow ci-n\pi$  decay channels. Careful dynamics calculations are required in order to understand the details.

#### IV. CONCLUSIONS

Spin-flip TDDFT is capable of correctly describing the topology of a conical intersection,<sup>16</sup> without increasing the computational cost relative to standard TDDFT. Results presented here for adenine suggest that this method affords minimum-energy crossing point geometries (along conical seams) that are in good agreement with geometries obtained from multireference wave function methods. In the present study, we have applied SF-TDDFT to examine the excited-state deactivation mechanisms of both gas-phase and hydrated uracil, by first locating the two most important MECPs, then optimizing reaction pathways connecting various stationary points with the MECPs, and finally confirming the energetics using coupled-cluster calculations. Based on the pathways thus obtained, we have assigned the time constants measured in time-resolved experiments.

Our calculations support the deactivation mechanism originally proposed in the experimental study by Hare et al.<sup>4</sup> Later theoretical studies<sup>9,27</sup> suggested the same mechanism with respect to the singlet manifold, namely, that ultrafast deactivation of the initially populated  $^1\pi\pi^*$  state occurs alongside formation of an longer-lived  $^1n\pi^*$  dark state whose energetics are sensitive to hydration. The present work presents optimized MECPs and minimum-energy pathways that were not computed in previous theoretical studies, which support the idea that a solvatochromatic blue-shift in the  $^1n\pi^*$  state decreases the barrier between  $S_{n\pi^*}$ -min and the  $ci$ - $n\pi$  MECP, effectively decreasing the dark-state lifetime in protic solvents.

The ultrafast decay component  $\tau_1 = 120$  fs that is measured experimentally<sup>4</sup> is assigned to direct relaxation from the first  $^1\pi\pi^*$  state to the ground state via conical intersection  $ci$ - $0\pi$ , whereas the slow component (" $\tau_4$ " in the notation of ref 4 and Figure 1, and measured to be  $\approx 24$  ps for aqueous uracil<sup>26</sup>) is assigned to indirect relaxation via the pathway  $^1\pi\pi^* \rightarrow ^1n\pi^* \rightarrow S_0$ . The lifetime of the dark  $^1n\pi^*$  state is observed to increase from tens of picoseconds in protic solvents to several nanoseconds in aprotic solvents,<sup>4</sup> and this behavior is ascribed to solvatochromatic shifts that serve to decrease a key activation barrier on the  $^1n\pi^*$  state. Finally, we find no evidence that trapping should occur on the  $^1\pi\pi^*$  state, either in the gas phase or in aqueous solution.

More generally, our results for both uracil and adenine suggest that SF-TDDFT can describe the excited state properties of nucleobases reasonably well. If we limit the discussion to relative energies of singlet excited states, then SF-TDDFT results for uracil agree very well with the CC2 results, although excitation energies with respect to  $S_0$  are overestimated with respect to both experiment and CC2. For uracil, this overestimation is largely corrected by SF-TDDFT calculations performed within the noncollinear formalism. This shift relative to  $S_0$  may be due to the relatively large fraction of Hartree–Fock exchange (50%) that is found to yield best results for collinear SF-TDDFT,<sup>17,20</sup> which has been suggested to be an artifact of the collinear formalism.<sup>24</sup> Noncollinear exchange–correlation kernels may therefore be better choices for future work, although gradients are not yet available. In any case, the low cost of SF-TDDFT makes its use promising for application to larger nucleic acid assemblies. In the present context, it is notable that uridine monophosphate exhibits a slow relaxation component of  $\approx 147$  ps in aqueous solution, as compared to 24 ps for aqueous uracil,<sup>26</sup> suggesting that theoretical comparisons involving larger systems would be useful.

One cautionary note concerning the present methodology, however, that is especially relevant in the context of ab initio molecular dynamics, is that to use SF-TDDFT one must identify and eliminate the  $M_s = 0$  component of the triplet from the singlet excitation manifold. In our hands, this has often proven difficult away from the Franck–Condon region, owing to significant spin contamination. Recently, Li et al.<sup>54</sup> introduced a spin-adapted formalism for the open-shell random phase approximation, using the tensor equation of motion formalism,<sup>55</sup> and this approach offers a potential solution to the spin contamination issue. Meanwhile, the formalism for computing analytic first-order nonadiabatic coupling vectors for linear-response TDDFT has been published,<sup>56,57</sup> and extension to SF-TDDFT is straightforward. This would obviate the need for the branching-plane updating algorithm that is used here, as MECP optimization could proceed directly along

the vectors  $\mathbf{g}^J$  and  $\mathbf{h}^J$ . Efforts to improve SF-TDDFT along these lines are underway in our group.

## ■ ASSOCIATED CONTENT

### Supporting Information

Cartesian coordinates of various optimized structures. This material is available free of charge via the Internet at <http://pubs.acs.org>.

## ■ AUTHOR INFORMATION

### Corresponding Author

\*E-mail: [herbert@chemistry.ohio-state.edu](mailto:herbert@chemistry.ohio-state.edu).

### Notes

The authors declare no competing financial interest.

## ■ ACKNOWLEDGMENTS

This work was supported by an NSF CAREER award (CHE-0748448). Calculations were performed at the Ohio Supercomputer Center under Project PAA-0003. J.M.H. is an Alfred P. Sloan Foundation fellow and a Camille Dreyfus Teacher-Scholar.

## ■ REFERENCES

- (1) Crespo-Hernández, C. E.; Cohen, B.; Hare, P. M.; Kohler, B. Ultrafast Excited-State Dynamics in Nucleic Acids. *Chem. Rev.* **2004**, *104*, 1977–2019.
- (2) Middleton, C. T.; de La Harpe, K.; Su, C.; Law, Y. K.; Crespo-Hernández, C. E.; Kohler, B. DNA Excited-State Dynamics: From Single Bases to the Double Helix. *Annu. Rev. Phys. Chem.* **2009**, *60*, 217–239.
- (3) He, Y.; Wu, C.; Kong, W. Photophysics of Methyl-Substituted Uracils and Thymine and Their Water Complexes in the Gas Phase. *J. Phys. Chem. A* **2004**, *108*, 943–949.
- (4) Hare, P. M.; Crespo-Hernández, C. E.; Kohler, B. Solvent-Dependent Photophysics of 1-Cyclohexyluracil: Ultrafast Branching in the Initial Bright State Leads Nonradiatively to the Electronic Ground State and a Long-Lived  $^1n\pi^*$  State. *J. Phys. Chem. B* **2006**, *110*, 18641–18650.
- (5) Kang, H.; Lee, K. T.; Jung, B.; Ko, Y. J.; Kim, S. S. Intrinsic Lifetimes of the Excited States of DNA and RNA Bases. *J. Am. Chem. Soc.* **2002**, *124*, 12958–12959.
- (6) Ullrich, S.; Schultz, T.; Zgierski, M. Z.; Stolow, A. Electronic Relaxation Dynamics in DNA and RNA Bases Studied by Time-Resolved Photoelectron Spectroscopy. *Phys. Chem. Chem. Phys.* **2004**, *6*, 2796–2801.
- (7) Matsika, S. Radiationless Decay of Excited States of Uracil through Conical Intersections. *J. Phys. Chem. A* **2004**, *108*, 7584–7590.
- (8) Epifanovsky, E.; Kowalski, K.; Fang, P.-D.; Valiev, M.; Matsika, S.; Krylov, A. I. On the Electronically Excited States of Uracil. *J. Phys. Chem. A* **2008**, *112*, 9983–9992.
- (9) Mercier, Y.; Santoro, F.; Reguero, M.; Improta, R. The Decay from the Dark  $n\pi^*$  Excited State in Uracil: An Integrated CASPT2/CASSCF and PCM/TD-DFT Study in the Gas Phase and in Water. *J. Phys. Chem. B* **2008**, *112*, 10769–10772.
- (10) Merchán, M.; Serrano-Andrés, L.; Robb, M. A.; Blancafort, L. Triplet-State Formation along the Ultrafast Decay of Excited Singlet Cytosine. *J. Am. Chem. Soc.* **2005**, *127*, 1820–1825.
- (11) Hudock, H. R.; Levine, B. G.; Thompson, A. L.; Satzger, H.; Townsend, D.; Gador, N.; Ullrich, S.; Stolow, A.; Martinez, T. J. Ab Initio Molecular Dynamics and Time-Resolved Photoelectron Spectroscopy of Electronically Excited Uracil and Thymine. *J. Phys. Chem. A* **2007**, *111*, 8500–8508.
- (12) Nachtigallová, D.; Aquino, A. J. A.; Szymczak, J. J.; Barbatti, M.; Hobza, P.; Lischka, H. Nonadiabatic Dynamics of Uracil: Population Splitting among Different Decay Mechanisms. *J. Phys. Chem. A* **2011**, *115*, 5247–5255.

- (13) Zelený, T.; Ruckebauer, M.; Aquino, A. J. A.; Müller, T.; Lankaš, F.; Dršata, T.; Hase, W. L.; Nachtigallova, D.; Lischka, H. Strikingly Different Effects of Hydrogen Bonding on the Photo-dynamics of Individual Nucleobases in DNA: Comparison of Guanine and Cytosine. *J. Am. Chem. Soc.* **2012**, *134*, 13662–13669.
- (14) Improt, R.; Barone, V.; Lami, A.; Santoro, F. Quantum Dynamics of the Ultrafast  $\pi\pi^*/n\pi^*$  Population Transfer in Uracil and 5-Fluoro-Uracil in Water and Acetonitrile. *J. Phys. Chem. B* **2009**, *113*, 14491–14503.
- (15) Borden, W. T.; Davidson, E. R. The Importance of Including Dynamic Electron Correlation in Ab Initio Calculations. *Acc. Chem. Res.* **1996**, *29*, 67–75.
- (16) Levine, B. G.; Ko, C.; Quenneville, J.; Martinez, T. J. Conical Intersections and Double Excitations in Time-Dependent Density Functional Theory. *Mol. Phys.* **2006**, *104*, 1039–1051.
- (17) Shao, Y.; Head-Gordon, M.; Krylov, A. I. The Spin-Flip Approach within Time-Dependent Density Functional Theory: Theory and Applications to Diradicals. *J. Chem. Phys.* **2003**, *118*, 4807–4818.
- (18) Wang, F.; Ziegler, T. Time-Dependent Density Functional Theory Based on a Noncollinear Formulation of the Exchange-Correlation Potential. *J. Chem. Phys.* **2004**, *121*, 12191:1–6.
- (19) Bernard, Y. A.; Shao, Y.; Krylov, A. I. General Formulation of Spin-Flip Time-Dependent Density Functional Theory Using Non-Collinear Kernels: Theory, Implementation, and Benchmarks. *J. Chem. Phys.* **2012**, *136*, 204103:1–17.
- (20) Minezawa, N.; Gordon, M. S. Optimizing Conical Intersections by Spin-Flip Density Functional Theory: Application to Ethylene. *J. Phys. Chem. A* **2009**, *113*, 12749–12753.
- (21) Minezawa, N.; Gordon, M. S. Photoisomerization of Stilbene: A Spin-Flip Density Functional Theory Study. *J. Phys. Chem. A* **2011**, *115*, 7901–7911.
- (22) Minezawa, N.; Gordon, M. S. Optimizing Conical Intersections of Solvated Molecules: The Combined Spin-Flip Density Functional Theory/Effective Fragment Potential Method. *J. Chem. Phys.* **2012**, *137*, 034116:1–12.
- (23) Harabuchi, Y.; Maeda, S.; Taketsugu, T.; Minezawa, N.; Morokuma, K. Automated Search for Minimum Energy Conical Intersection Geometries between the Lowest Two Singlet States  $S_0/S_1$ -MECs by the Spin-Flip TDDFT Method. *J. Chem. Theory Comput.* **2013**, *9*, 4116–4123.
- (24) Huix-Rotlant, M.; Natarajan, B.; Ipatov, A.; Wawire, C. M.; Deutsch, T.; Casida, M. E. Assessment of Noncollinear Spin-Flip Tamm–Dancoff Approximation Time-Dependent Density-Functional Theory for the Photochemical Ring-Opening of Oxirane. *Phys. Chem. Chem. Phys.* **2010**, *12*, 12811–12825.
- (25) He, Y.; Wu, C.; Kong, W. Decay Pathways of Thymine and Methyl-Substituted Uracil and Thymine in the Gas Phase. *J. Phys. Chem. A* **2003**, *107*, 5145–5148.
- (26) Hare, P. M.; Crespo-Hernández, C. E.; Kohler, B. Internal Conversion to the Electronic Ground State Occurs via Two Distinct Pathways for Pyrimidine Bases in Aqueous Solution. *Proc. Natl. Acad. Sci. U.S.A.* **2007**, *104*, 435–440.
- (27) Yoshikawa, A.; Matsika, S. Excited Electronic States and Photophysics of Uracil–Water Complexes. *Chem. Phys.* **2008**, *347*, 393–404.
- (28) Santoro, F.; Barone, V.; Gustavsson, T.; Improt, R. Solvent Effect on the Singlet Excited-State Lifetimes of Nucleic Acid Bases: A Computational Study of 5-Fluorouracil and Uracil in Acetonitrile and Water. *J. Am. Chem. Soc.* **2006**, *128*, 16312–16322.
- (29) Gustavsson, T.; Sarkar, N.; Lazzarotto, E.; Markovitsi, D.; Barone, V.; Improt, R. Solvent Effect on the Singlet Excited-State Dynamics of 5-Fluorouracil in Acetonitrile as Compared with Water. *J. Phys. Chem. B* **2006**, *110*, 12843–12847.
- (30) Gustavsson, T.; Bányász, A.; Lazzarotto, E.; Markovitsi, D.; Scalmani, G.; Frisch, M. J.; Barone, V.; Improt, R. Singlet Excited-State Behavior of Uracil and Thymine in Aqueous Solution: A Combined Experimental and Computational Study of 11 Uracil Derivatives. *J. Am. Chem. Soc.* **2006**, *128*, 607–619.
- (31) Salet, C.; Bensasson, R.; Becker, R. S. Triplet Excited States of Pyrimidine Nucleosides and Nucleotides. *Photochem. Photobiol.* **1979**, *30*, 325–329.
- (32) Maeda, S.; Ohno, K.; Morokuma, K. Updated Branching Plane for Finding Conical Intersections without Coupling Derivative Vectors. *J. Chem. Theory Comput.* **2010**, *6*, 1538–1545.
- (33) Bearpark, M. J.; Robb, M. A.; Schlegel, H. B. A Direct Method for the Location of the Lowest Energy Point on a Potential Surface Crossing. *Chem. Phys. Lett.* **1994**, *223*, 269–274.
- (34) Sicilia, F.; Blancafort, L.; Bearpark, M. J.; Robb, M. A. New Algorithms for Optimizing and Linking Conical Intersection Points. *J. Chem. Theory Comput.* **2008**, *4*, 257–266.
- (35) Levine, B. G.; Coe, J. D.; Martinez, T. J. Optimizing Conical Intersections without Derivative Coupling Vectors: Application to Multistate Multireference Second-Order Perturbation Theory (MS-CASPT2). *J. Phys. Chem. B* **2008**, *112*, 405–413.
- (36) Becke, A. D. Density-Functional Exchange-Energy Approximation with Correct Asymptotic Behavior. *Phys. Rev. A* **1988**, *38*, 3098–3100.
- (37) Lee, C.; Yang, W.; Parr, R. G. Development of the Colle-Salvetti Correlation-Energy Formula into a Functional of the Electron Density. *Phys. Rev. B* **1988**, *37*, 785–789.
- (38) Barbatti, M.; Lischka, H. Nonadiabatic Deactivation of 9H-Adenine: A Comprehensive Picture Based on Mixed Quantum–Classical Dynamics. *J. Am. Chem. Soc.* **2008**, *130*, 6831–6839.
- (39) Lange, A. W.; Herbert, J. M. Polarizable Continuum Reaction-Field Solvation Models Affording Smooth Potential Energy Surfaces. *J. Phys. Chem. Lett.* **2010**, *1*, 556–561.
- (40) Lange, A. W.; Herbert, J. M. A Smooth, Non-Singular, and Faithful Discretization Scheme for Polarizable Continuum Models: The Switching/Gaussian Approach. *J. Chem. Phys.* **2010**, *133*, 244111:1–18.
- (41) Peters, B.; Heyden, A.; Bell, A. T.; Chakraborty, A. A Growing String Method for Determining Transition States: Comparison to the Nudged Elastic Band and String Methods. *J. Chem. Phys.* **2004**, *120*, 7877–7886.
- (42) Behn, A.; Zimmerman, P. M.; Bell, A. T.; Head-Gordon, M. Efficient Exploration of Reaction Paths via a Freezing String Method. *J. Chem. Phys.* **2011**, *135*, 224108:1–9.
- (43) Rohrdanz, M. A.; Martins, K. M.; Herbert, J. M. A Long-Range-Corrected Density Functional That Performs Well for Both Ground-State Properties and Time-Dependent Density Functional Theory Excitation Energies, Including Charge-Transfer Excited States. *J. Chem. Phys.* **2009**, *130*, 054112:1–8.
- (44) TURBOMOLE, V. 6.3.1, a development of University of Karlsruhe and Forschungszentrum Karlsruhe GmbH, 1989–2007, TURBOMOLE GmbH, Germany, 2007; available from <http://www.turbomole.com>.
- (45) Shao, Y.; Fusti-Molnar, L.; Jung, Y.; Kussmann, J.; Ochsenfeld, C.; Brown, S. T.; Gilbert, A. T. B.; Slipchenko, L. V.; Levchenko, S. V.; O'Neill, D. P.; et al. Advances in Methods and Algorithms in a Modern Quantum Chemistry Program Package. *Phys. Chem. Chem. Phys.* **2006**, *8*, 3172–3191.
- (46) Krylov, A. I.; Gill, P. M. W. Q-Chem: An Engine for Innovation. *WIREs Comput. Mol. Sci.* **2013**, *3*, 317–326.
- (47) Taylor, R.; Kennard, O. The Molecular Structures of Nucleosides and Nucleotides: Part 1. The Influence of Protonation on the Geometries of Nucleic Acid Constituents. *J. Mol. Struct.* **1982**, *78*, 1–28.
- (48) Fleig, T.; Knecht, S.; Hättig, C. Quantum-Chemical Investigation of the Structures and Electronic Spectra of the Nucleic Acid Bases at the Coupled Cluster CC2 Level. *J. Phys. Chem. A* **2007**, *111*, 5482–5491.
- (49) Kistler, K. A.; Matsika, S. Solvatochromatic Shifts of Uracil and Cytosine Using a Combined Multireference Configuration Interaction/Molecular Dynamics Approach and the Fragment Molecular Orbital Method. *J. Am. Chem. Soc.* **2009**, *131*, 12396–12403.

- (50) DeFusco, A.; Ivancic, J.; Schmidt, M. W.; Gordon, M. S. Solvent-Induced Shifts in Electronic Spectra of Uracil. *J. Phys. Chem. A* **2011**, *115*, 4574–4582.
- (51) Olsen, J. M.; Aidas, K.; Mikkelsen, K. V.; Kongsted, J. Solvatochromatic Shifts in Uracil: A Combined MD-QM/MM Study. *J. Chem. Theory Comput.* **2009**, *6*, 249–256.
- (52) Etinski, M.; Marian, C. M. Ab Initio Investigation of the Methylation and Hydration Effects on the Electronic Spectra of Uracil and Thymine. *Phys. Chem. Chem. Phys.* **2010**, *12*, 4915–4923.
- (53) Merchán, M.; González-Luque, R.; Climent, T.; Serrano-Andrés, L. Unified Model for the Ultrafast Decay of Pyrimidine Nucleobases. *J. Phys. Chem. B* **2006**, *110*, 26471–26476.
- (54) Li, Z.; Liu, W. Spin-Adapted Open-Shell Random Phase Approximation and Time-Dependent Density Functional Theory. I. *J. Chem. Phys.* **2010**, *133*, 064106:1–22.
- (55) Rowe, D. J.; Ngo-Trong, C. Tensor Equations of Motion for the Excitations of Rotationally Invariant or Charge-Independent Systems. *Rev. Mod. Phys.* **1975**, *47*, 471–485.
- (56) Chernyak, V.; Mukamel, S. Density-Matrix Representation of Nonadiabatic Couplings in Time-Dependent Density Functional (TDDFT) Theories. *J. Chem. Phys.* **2000**, *112*, 3572–3579.
- (57) Send, R.; Furche, F. First-Order Nonadiabatic Couplings from Time-Dependent Hybrid Density Functional Response Theory: Consistent Formalism, Implementation, and Performance. *J. Chem. Phys.* **2010**, *132*, 044107:1–12.